Supporting Information

When can an excitonic insulator be a purely electronic ferroelectric? Symmetry conditions tested on monolayer $Ta_2Pd_3Te_5$

Gábor I. Csonka, Hong Tang and Adrienn Ruzsinszky

Department of Physics and Engineering Physics, Tulane University, New Orleans, LA 70118, USA

S1. Comparison of the bulk r^{2}SCAN+rVV10 dispersion with ARPES

Figure S1 compares the r^{2}SCAN+rVV10 [1, 2] dispersion of bulk $Ta_2Pd_3Te_5$ along Y–Γ–Y, the chain direction, with the ARPES data of Zhang *et al.* measured with 30 eV (top row) and 67 eV (bottom row) photons [3]. In the normal state at 350 K [(a), (d)] the calculation reproduces the m-shaped valence bands and the electron-like conduction band at Γ. On cooling [(b), (c), (e), (f)], the measured conduction-band minimum shifts upward and a gap opens that the calculation does not contain, the signature of the low-temperature insulating state that density functional theory does not capture.

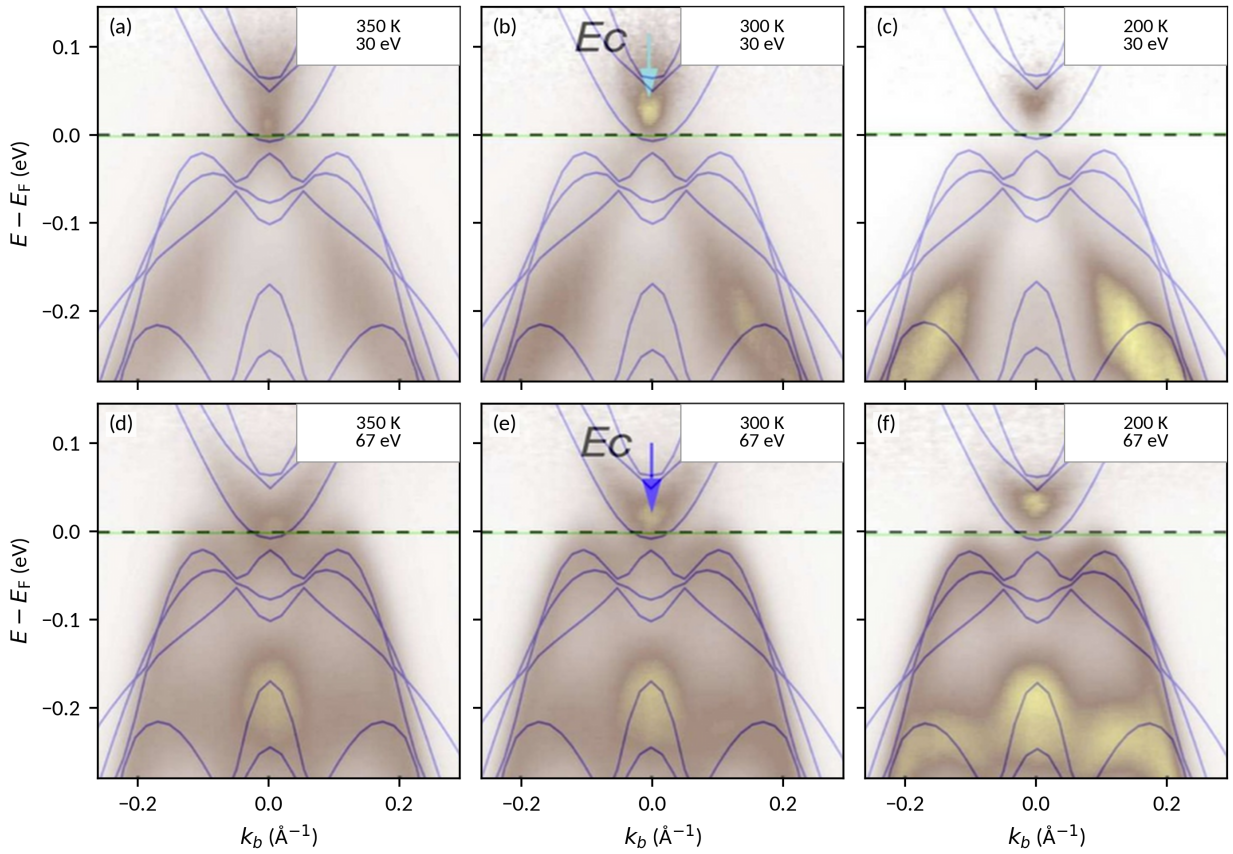


Fig. S1. Bulk $Ta_2Pd_3Te_5$ band structure along Y–Γ–Y calculated with r^{2}SCAN+rVV10 (blue lines), superimposed on ARPES intensity measured along the chain direction at $k_c = 0$ at 350, 300 and 200 K with 30 eV photons (a)–(c) and 67 eV photons (d)–(f). Energies are referenced to the respective Fermi levels (dashed line). The arrows labelled E_c in (b) and (e) mark the measured conduction-band minimum, as in the original figure. ARPES data reproduced from Figs. 2(a2)–(a4) and 2(b2)–(b4) of Ref. [3] under the Creative Commons Attribution 4.0 International license; calculated bands overlaid, temperature labels, panel labels and axes redrawn.

S2. Symmetry operators and channel-resolved mean field

Operators. In the setting of the Wannier90 cell, $Pmmn$ contains the mirrors σ_x and σ_y through the origin, the rotation C_{2z}, and four operations carrying the translation $\boldsymbol{\tau} = (a/2, b/2, 0)$: the inversion I, the screws 2_{1x} and 2_{1y} and the glide n_z. An operation $g = \{R|\boldsymbol{\tau}_g\}$ maps the centre of Wannier function i onto the centre of a function $p(i)$ of the same orbital type, up to a lattice vector $\mathbf{T}_i$; $s_i = \pm 1$ is the parity of the orbital under R. The representation on Bloch sums is

$$U_g(\mathbf{k})_{p(i),i} = s_i \, e^{-2\pi i \, g\mathbf{k}\cdot\mathbf{T}_i}, \tag{1}$$

and the residual r_g defined in the Methods of the main text is evaluated on the 36×8 mesh, along the X–Γ–Y path and at six random $\mathbf{k}$ points. Because $H_0(\mathbf{k})$ is a finite Fourier series, the residual matrix has exact lattice Fourier coefficients $\Delta_g(\mathbf{R})$, obtained here by a fast Fourier transform on a grid larger than their range, and $r_g \leq \sum_{\mathbf{R}} \max |\Delta_g(\mathbf{R})|$ at every $\mathbf{k}$. For the three exact operations of the maximally localized model this bound is 22.7, 28.6 and 37.1 meV (σ_y, n_z and 2_{1x}), against at least 530 meV for the broken operations at sampled points.

Bond operators and interaction. Each Ta–X bond $(c, v, \mathbf{R})$ with Wannier centres closer than r_c contributes two Hermitian operators,

$$\hat{O}^S = \tfrac{1}{\sqrt{2}} \left(c^\dagger_{c,0} c_{v,\mathbf{R}} + \text{h.c.} \right), \qquad \hat{O}^A = \tfrac{i}{\sqrt{2}} \left(c^\dagger_{c,0} c_{v,\mathbf{R}} - \text{h.c.} \right), \tag{2}$$

and the interaction is $H_{\text{int}} = -\frac{V_0}{2} \sum_i (\hat{O}_i - \langle \hat{O}_i \rangle_0)^2$, with $\langle \cdot \rangle_0$ the normal-state expectation value. Subtracting $\langle \hat{O}_i \rangle_0$ prevents the hybridization already present in H_0 from acting as a source term.

Mean field. For field amplitudes $\boldsymbol{\lambda}$ the mean-field free energy is

$$F(\boldsymbol{\lambda}) = E_{\text{b}}(\boldsymbol{\lambda}) - \boldsymbol{\lambda} \cdot \mathbf{g}_0 + \frac{|\boldsymbol{\lambda}|^2}{2V_0}, \tag{3}$$

where E_{b} is the band energy of $H_0 + \sum_i \lambda_i \hat{O}_i$ at fixed filling (12 of 16 bands) and $\mathbf{g}_0 = \langle \hat{\mathbf{O}} \rangle_0$. Stationarity gives the gap equation $\boldsymbol{\lambda} = -V_0 \, \mathcal{P}_\Gamma (\mathbf{g} - \mathbf{g}_0)$ with the channel projector

$$\mathcal{P}_\Gamma = \frac{1}{|G|} \sum_{g \in G} \chi_\Gamma(g) \, D(g), \tag{4}$$

where G contains only the operations that pass the symmetry test and $D(g)$ is the signed permutation of the bond operators induced by U_g.

Critical coupling. Expanding F to second order in $\boldsymbol{\lambda}$ gives the static $\mathbf{q} = 0$ pair susceptibility

$$\chi_{ij} = 2 \sum_{\mathbf{k}} w_{\mathbf{k}} \sum_{n \in \text{occ}} \sum_{m \in \text{emp}} \frac{\text{Re} \left[\langle m|\hat{O}_i|n\rangle \langle n|\hat{O}_j|m\rangle \right]}{\varepsilon_m - \varepsilon_n}, \tag{5}$$

and the channel becomes unstable at $V_0^c = 1/\lambda_{\max}(\mathcal{P}_\Gamma \chi \mathcal{P}_\Gamma)$.

Interband velocity matrix elements (Fig. 3(b) of the main text). The velocity operator is $v_x(\mathbf{k}) = \partial H_0 / \partial k_x = \sum_{\mathbf{R}} i R_x \, H_0(\mathbf{R}) \, e^{i\mathbf{k}\cdot\mathbf{R}}$; intra-cell position matrix elements of the Wannier functions are omitted, so magnitudes are approximate while zeros imposed by symmetry are exact. The bands that are v_1, c_1 and c_2 at Γ are followed outward by maximal eigenvector overlap. Before each step, groups of states within 5 meV are diagonalized in a linear combination of the operations that are exact at that $\mathbf{k}$ (n_z everywhere; σ_y and 2_{1x} on Γ–X), so that crossings between different symmetry

sectors are not mistaken for mixing. Within 0.12 Å^{-1} of X the followed valence band lies among three bands within 6 meV, and the curves are omitted there and next to Y.

Convergence. V_0^c changes by less than 0.3% between 12×4 and 72×16 meshes; the reported values use 36×8. Self-consistent solutions of the gap equation with linear mixing, started from several random seeds in each channel, converge to $\boldsymbol{\lambda} = 0$ below V_0^c. The bond cutoffs $r_c = 3.4$, 4.0 and 4.6 Å include 16, 20 and 24 Ta–X bond pairs.

S3. Supplementary File S1: interactive 3D version of Fig. 4

Supplementary File S1 (`fig4_interactive.html`) shows the Wannier centres, projection seeds, atoms and σ_x mirror planes of Fig. 4 in a rotatable 3D view that opens in any web browser without additional software. Hovering over a Wannier centre displays its orbital, spread, rms radius, offset from its seed atom and distance to the nearest σ_x plane. Buttons select four camera views and switch between true proportions and an x axis stretched three times, which makes the σ_x-breaking offsets visible; legend entries show or hide each layer, including the Ta–X and Pd–Te bonds and spheres indicating the extent of each Wannier function (0.3 times its rms radius). The file and the script that generates it are part of the data repository.

S4. Robustness of the channel ordering across Wannier models

The disentangled subspace and the gauge of a Wannier Hamiltonian are choices, so the channel ordering of Fig. 5 is tested on four Wannier models of the same monolayer (Table S1). Three are built from the VASP r^{2}SCAN calculation of the paper with Wannier90 and the same 16 projections: the maximally localized model used in the main text; projection-only Wannier functions (`num_iter = 0`) on the same disentanglement windows, which isolates the effect of maximal localization; and projection-only functions with the frozen window raised to -2.05 eV, so that v_1, c_1 and c_2 are frozen. The fourth is a symmetry-adapted model (site symmetry imposed during disentanglement and localization [4]) built from a Quantum ESPRESSO [5, 6] r^{2}SCAN calculation (Libxc [7]) with optimized norm-conserving Vanderbilt pseudopotentials [8] from the PseudoDojo table, generated with PBE [9], a kinetic-energy cutoff of 90 Ry, a $28 \times 6 \times 1$ mesh and the relaxed structure of the main text; Wannier90 does not allow a frozen window with site symmetry, so this model has none. All thresholds are evaluated with the program of Sec. S2 at the bond cutoff $r_c = 3.4$ Å, with the filling given by the position of v_1 in each model.

Table S1. Four Wannier models of monolayer $Ta_2Pd_3Te_5$. Exact group: number of $Pmmn$ operations with residual $r_g < 20$ meV on the 36×8 mesh and the X–Γ–Y path; in parentheses, operations kept only approximately. In the two projection-only models the channels are projected with these approximate operations, so their thresholds rank merged channels approximately. Gap: direct gap at Γ at the stated filling; the r^{2}SCAN DFT gap is 130 meV (VASP) and 145 meV (Quantum ESPRESSO). V_0^c: critical coupling of the channel containing A_u and of the channel containing B_{3u} at $r_c = 3.4$ Å.

Model	Exact group	Filling	Gap at Γ	Channels	$V_0^c(A_u)$	$V_0^c(B_{3u})$
VASP, maximally localized (main text)	4	12	108 meV	$A_u \oplus B_{3g}$, $A_g \oplus B_{3u}$	1.42 eV	1.56 eV
VASP, projection-only	1 (3 at 46–77 meV)	12	108 meV	$A_u \oplus B_{3g}$, $A_g \oplus B_{3u}$ (approx.)	1.37 eV	1.49 eV
VASP, projection-only, frozen window raised	1 (σ_z at 96 meV)	10	130 meV	groups of four (approx.)	1.14 eV	1.21 eV
QE, symmetry-adapted	8	12	semimetallic	all separated	1.39 eV	1.99 eV

On the same subspace, projection-only Wannier functions break the same four operations as the maximally localized model, by 0.56 eV, and keep the other three only approximately (46–77 meV): maximal localization does not cause the loss of those four operations; the disentanglement does. Raising the frozen window reproduces the DFT band edges exactly (v_1, c_1 and c_2 at Γ to within 1 meV) but breaks every operation, the least broken being σ_z at 96 meV. The symmetry-adapted model keeps all eight operations (residuals below 9 meV) and separates every channel: $V_0^c(A_u) = 1.39$ eV (its time-reversal-odd part; the ordinary singlet follows at 1.41 eV), followed by B_{2g} at 1.43 eV, B_{1g} at 1.90 eV, B_{3u} at 1.99 eV, B_{3g} at 2.51 eV and A_g at 2.87 eV. Without a frozen window its band edges deviate from the DFT bands by 30–140 meV and its bands overlap, so it separates the A_u channel from the polar singlet but fixes neither the thresholds nor the order of the three lowest channels, which lie within 3%. In all four models the channel containing A_u has the lower critical coupling. A model that is both symmetric and correct at the band edges requires a symmetry-constrained disentanglement with a frozen window, which Wannier90 does not provide.

The symmetry loss of the third model has a representation-theoretic origin. A frozen window must be spanned exactly by the Wannier functions, so at every **k** the irreducible representations of the frozen states must be contained in those the basis carries. The window from -3.1 to -2.05 eV holds seven states at Γ: v_1, c_1, c_2 and four deeper valence states. Among them are two states of one irreducible representation of the little group of Γ, while the 16-function basis (four Ta d_{z^2}, ten Te p_x, two Pd d_{xz}) induces only one state of that representation. No symmetric 16-function model can therefore contain this window; Wannier90, which does not test the condition, reproduces the frozen states and gives up the symmetry instead. A frozen window restricted to v_1, c_1 and c_2 (-2.45 to -2.10 eV) satisfies the condition at every **k** of the mesh, as checked with the irreducible-representation test of WannierBerri [10].

References

[1] J. W. Furness, A. D. Kaplan, J. Ning, J. P. Perdew, and J. Sun. Accurate and numerically efficient r^{2}SCAN meta-generalized gradient approximation. *J. Phys. Chem. Lett.*, 11:8208, 2020. doi: 10.1021/acs.jpclett.0c02405.

[2] J. Ning et al. Workhorse minimally empirical dispersion-corrected density functional with tests for weakly bound systems: r^{2}SCAN+rVV10. *Phys. Rev. B*, 106:075422, 2022. doi: 10.1103/PhysRevB.106.075422.

[3] P. Zhang et al. Spontaneous gap opening and potential excitonic states in an ideal Dirac semimetal $Ta_2Pd_3Te_5$. *Phys. Rev. X*, 14:011047, 2024. doi: 10.1103/PhysRevX.14.011047.

[4] R. Sakuma. Symmetry-adapted Wannier functions in the maximal localization procedure. *Phys. Rev. B*, 87:235109, 2013. doi: 10.1103/PhysRevB.87.235109.

[5] P. Giannozzi et al. QUANTUM ESPRESSO: a modular and open-source software project for quantum simulations of materials. *J. Phys.: Condens. Matter*, 21:395502, 2009. doi: 10.1088/0953-8984/21/39/395502.

[6] P. Giannozzi et al. Advanced capabilities for materials modelling with Quantum ESPRESSO. *J. Phys.: Condens. Matter*, 29:465901, 2017. doi: 10.1088/1361-648X/aa8f79.

[7] S. Lehtola, C. Steigemann, M. J. T. Oliveira, and M. A. L. Marques. Recent developments in Libxc: a comprehensive library of functionals for density functional theory. *SoftwareX*, 7: 1–5, 2018. doi: 10.1016/j.softx.2017.11.002.

[8] D. R. Hamann. Optimized norm-conserving Vanderbilt pseudopotentials. *Phys. Rev. B*, 88: 085117, 2013. doi: 10.1103/PhysRevB.88.085117.

[9] M. J. van Setten, M. Giantomassi, E. Bousquet, M. J. Verstraete, D. R. Hamann, X. Gonze, and G.-M. Rignanese. The PseudoDojo: Training and grading a 85 element optimized norm-conserving pseudopotential table. *Comput. Phys. Commun.*, 226:39–54, 2018. doi: 10.1016/j.cpc.2018.01.012.

[10] WannierBerri developers. WannierBerri documentation. Online documentation, 2026. URL `https://docs.wannier-berri.org`. Accessed 30 October 2026.